COMPDYN 2011
III ECCOMAS Thematic Conference on
Computational Methods in Structural Dynamics and Earthquake Engineering
M. Papadrakakis, M. Fragiadakis, V. Plevris (eds.)
Corfu, Greece, 25–28 May 2011

# SEISMIC DAMAGE ANALYSIS OF REINFORCED CONCRETE STRUCTURES WITH SUBSTANDARD DETAILING

**Panagiotis E. Mergos**[1], **Andreas J. Kappos**[1]

[1] Laboratory of Concrete and Masonry Structures, Department of Civil Engineering,
Aristotle University of Thessaloniki, 54124, Greece
e-mail: panmerg@yahoo.com; ajkap@civil.auth.gr

**Keywords:** Finite element, Reinforced Concrete, Shear-Flexure interaction, Bond-slip, Substandard detailing

**Abstract.** *The goal of this study is to investigate seismic behaviour of existing R/C buildings designed and constructed in accordance with standards that do not meet current seismic code requirements. In these structures, not only flexure, but also shear and bond-slip deformation mechanisms need to be considered separately and in combination. To serve this goal, a finite element model developed previously by the writers for individual non-ductile beam-column members is extended herein in order to cope with inelastic seismic analysis of complete planar R/C frames. The proposed finite element is able to capture gradual spread of inelastic flexural and shear deformations as well as their interaction in the end regions of R/C members. Additionally, it is capable of predicting shear failures caused by degradation of shear strength in the plastic hinges of R/C elements, as well as pullout failures caused by inadequate anchorage of the reinforcement in the joint regions. The finite element is fully implemented in the general inelastic finite element code IDARC2D. Then, the numerical model is calibrated against experimental data coming from three experimental plane frame structures with non-ductile detailing. It is shown that, in all cases, satisfactory correlation is established between the model predictions and the experimental evidence. The analytical results are in agreement with the experimental values in terms of stiffness, strength and displacement demands. The failure mechanism is predicted accurately for all experimental specimens. Finally, parametric studies illustrate the significance of each deformation mechanism in the seismic response of the experimental frames. It is concluded, that all deformation mechanisms, as well as their interaction, should be taken into consideration in order to predict reliably seismic damage of R/C structures with substandard detailing.*

## 1 INTRODUCTION

The vast majority of existing reinforced concrete (R/C) buildings was constructed prior to the development of modern seismic code provisions. The deficient design makes their structural elements susceptible to axial-flexural, shear or bond types of failure, which subsequently may lead to severe damage or collapse of the building.

Current research on seismic assessment of R/C structures is focused primarily on flexural response. Deformations caused by shear and bond-slip related mechanisms are either ignored or lumped into flexure. However, the necessary assumptions inherent to both of these approaches may drive the assessment procedure to erroneous results. This is especially the case for 'old type' existing R/C structures, where shear and bond types of failure cannot be precluded, due to the absence of ductile detailing and capacity design.

A significant number of analytical efforts have placed emphasis on seismic response of non-ductile R/C buildings. Among them, several studies [1-3] have demonstrated the necessity for treating individual deformation components (i.e. flexure, shear, anchorage bond-slip) in a distinct manner.

In this study, a finite element developed previously by the writers [4-7] for examining inelastic response of individual R/C beam-column members is extended herein to deal with seismic damage analysis of complete R/C frames with substandard detailing. The novel feature of the proposed finite element is the fact that it is capable of modelling gradual spread of inelastic flexural and shear deformations as well as their interaction in the end regions of R/C members. Furthermore, it has the ability of predicting shear failures caused by degradation of shear strength in the plastic hinges of R/C elements, as well as pullout failures caused by inadequate anchorage of the reinforcement in the joint regions.

The paper starts with a brief overview of the finite element model. Emphasis is placed on the abilities of the numerical model to predict brittle types of local failure (i.e. shear and bond). Moreover, the necessary alterations to the nonlinear solution algorithms are discussed in order for the proposed beam-column element to be fully implemented in a general inelastic damage analysis finite element code.

Then, with the aim to verify the capabilities of the proposed numerical model to reproduce all of the aforementioned phenomena strongly related to R/C buildings with deficient configuration, the proposed finite element is applied to the analysis of three well documented R/C frame specimens subjected to cyclic or seismic loading. Analytical results are compared with experimental recordings. It is shown that the numerical model is able to capture sufficiently experimental response in terms of strength, stiffness and displacements and to predict reliably the prevailing mode of failure for each specimen.

Finally, parametric analyses illustrate the relative importance of each deformation mechanism in the response of the examined specimens in the elastic and inelastic range. It is proven that proper modelling of all flexibility components, as well as their interaction, is a substantial prerequisite for reliable predictions of seismic response of R/C frames built with inadequate ductility capacity.

## 2 FINITE ELEMENT MODEL

The proposed, member-type, finite element is based on the flexibility method and belongs to the class of phenomenological models. It consists of three sub-elements representing flexural, shear, and anchorage bond-slip response (Fig. 1). The total flexibility of the finite element is calculated as the sum of the flexibilities of its sub-elements and can be inverted to produce the element stiffness matrix. Hence, it is

$$F_b = F^{fl} + F^{sh} + F^{sl} \tag{1}$$

$$K_b = F^{-1} \tag{2}$$

Where, $F_b$, $F^{fl}$, $F^{sh}$, $F^{sl}$ are the basic total, flexural, shear and anchorage slip, respectively, tangent flexibility matrices. $K_b$ is the basic tangent stiffness matrix of the element, connecting incremental moments $\Delta M_A$, $\Delta M_B$ and rotations $\Delta\theta_A$, $\Delta\theta_B$ at the element flexible ends A and B respectively, with the following equation

$$\begin{bmatrix} \Delta M_A \\ \Delta M_B \end{bmatrix} = K_b \cdot \begin{bmatrix} \Delta\theta_A \\ \Delta\theta_B \end{bmatrix} \tag{3}$$

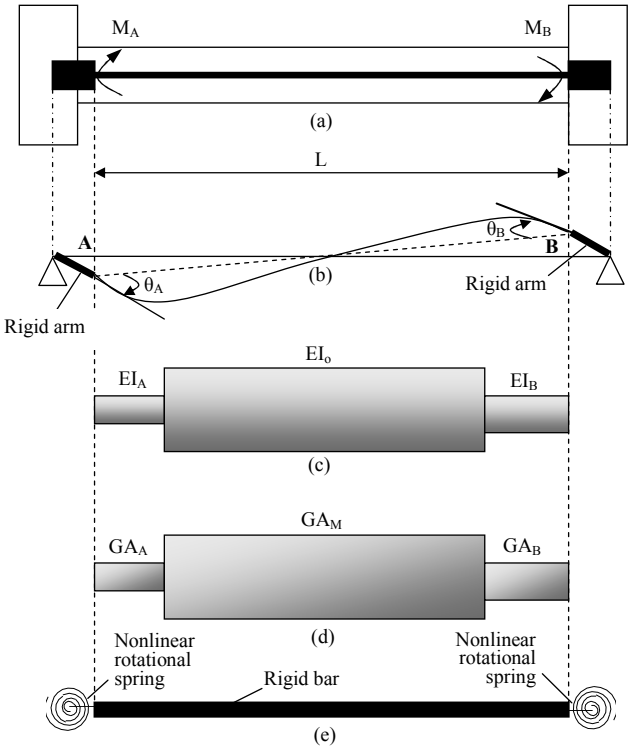


Figure 1: Proposed finite element model: a) geometry of R/C member; b) beam-column finite element with rigid arms; c) flexural sub-element; d) shear sub-element, e) anchorage bond-slip sub-element.

The local stiffness matrix $K_e$, relating displacements and forces at the element joints, is easily determined following standard structural analysis procedures. The components of the examined finite element, as well as their interaction, are described in the following sections.

### 2.1 Flexural Sub-Element

This sub-element (Fig. 1c) is used for modelling flexural behaviour of an R/C member before and after yielding of the longitudinal reinforcement. It consists of a set of rules governing the hysteretic moment-curvature (M-φ) response of the member end sections and a spread inelasticity model describing flexural stiffness distribution along the entire member.

M-φ hysteretic model (Fig. 2) is composed by the skeleton curve and a set of rules determining response during loading, unloading and reloading. M-φ envelope curve is derived by section analysis and appropriate bilinearization. Loading response is assumed to follow the bilinear envelope curve. Unloading is based on the respective Sivaselvan & Reinhorn [8] hys-

teretic rule adjusted for mild stiffness degradation. Reloading aims at the point with previous maximum excursion in the opposite direction.

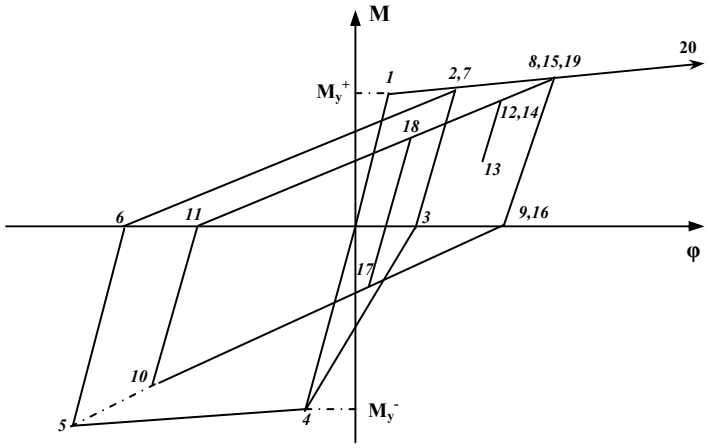


Figure 2: M-φ hysteretic model

In order to capture variation of section flexural stiffness along the concrete member, a gradual spread inelasticity model is assigned [9]. The stiffness distribution along the member is assumed to have one of the shapes shown in Fig. 3, where L is the length of the member; $EI_A$ and $EI_B$ are the current flexural rigidities of the sections at the ends A and B, respectively; $EI_o$ is the stiffness at the intermediate part of the element; $\alpha_A$ and $\alpha_B$ are the yield penetration coefficients. The flexural rigidities $EI_A$ and $EI_B$ are determined from the M-φ hysteretic relationship of the corresponding end sections. The yield penetration coefficients specify the proportion of the element where the acting moment is greater than the end-section yield moment. These coefficients are first calculated for the current moment distribution and then compared with the previous maximum penetration lengths.

Stiffness distribution inside the inelastic zone depends on the loading state of the end section hysteretic response. In particular, Fig. 4 illustrates hysteretic response of four discrete sections located inside the plastic hinge region. It can be seen that when all sections remain in the strain hardening branch (loading state), flexural stiffness remains constant in the inelastic zone. However, in the unloading and reloading state, stiffness varies from a minimum value (corresponding to the end section) to a maximum value, which is equal to $EI_o$. Hence, under the general assumption that the loading state of all sections of the yielded region remains the same, it may be considered that when M-φ end section hysteretic response is on the strain hardening branch, stiffness distribution remains uniform in the inelastic zone. In the case where end-section M-φ behaviour is in the unloading or reloading state, it is assumed that the stiffness varies linearly from $EI_A$ ($EI_B$) to $EI_o$.

Having established the stiffness distribution along the R/C member at each step of the analysis, the coefficients of the flexibility matrix of the flexural sub-element can be derived from the general Eq. (4) and Table 1, determined by applying the principle of virtual work.

$$f_{ij} = \frac{L}{12EI_o}\left(c_o + c_A \cdot \gamma_A + c_B \cdot \gamma_B\right);\ \gamma_A = \frac{EI_o}{EI_A} - 1;\ \gamma_B = \frac{EI_o}{EI_B} - 1 \tag{4}$$

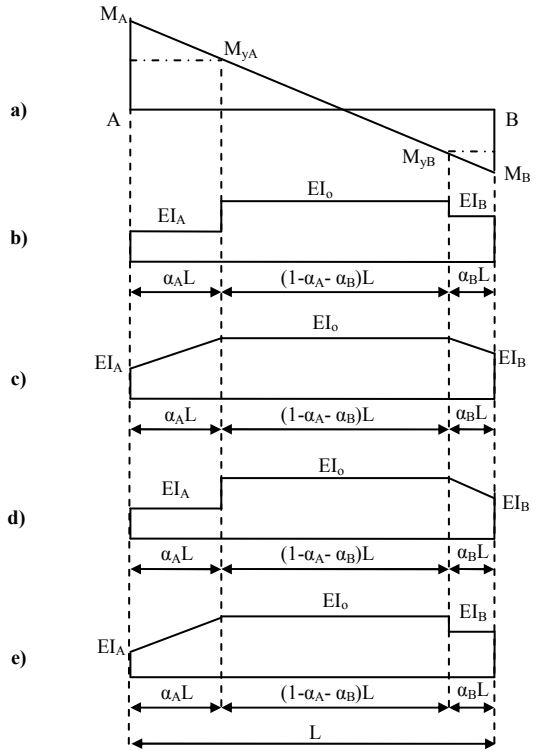


Figure 3: Element a) bending moment diagram; b) stiffness distribution when ends A and B are in the loading state; c) stiffness distribution when ends A and B are in the unloading or reloading state; d) stiffness distribution when end A is in the loading and end B is in the unloading or reloading state; e) stiffness distribution when end A is in the unloading or reloading state and end B is in the loading state.

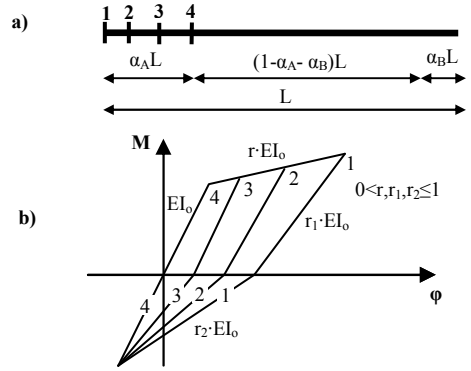


Figure 4: M-φ hysteretic response of four individual sections inside the plastic hinge region.

| Flexibility matrix coefficient | Stiffness distribution | $c_o$ | $c_A$ | $c_B$ |
|---|---|---|---|---|
| $f_{11}$ | Fig. 2b | 4 | $12\alpha_A -12\alpha_A^2+4\alpha_A^3$ | $4\alpha_B^3$ |
| $f_{12}$ | Fig. 2b | 4 | $4\alpha_A^3$ | $12\alpha_B -12\alpha_B^2+4\alpha_B^3$ |
| $f_{22}$ | Fig. 2b | -2 | $4\alpha_A^3-6\alpha_A^2$ | $4\alpha_B^3-6\alpha_B^2$ |
| $f_{11}$ | Fig. 2c | 4 | $6\alpha_A -4\alpha_A^2+\alpha_A^3$ | $\alpha_B^3$ |
| $f_{12}$ | Fig. 2c | 4 | $\alpha_A^3$ | $6\alpha_B -4\alpha_B^2+\alpha_B^3$ |
| $f_{22}$ | Fig. 2c | -2 | $\alpha_A^3-2\alpha_A^2$ | $\alpha_B^3-2\alpha_B^2$ |
| $f_{11}$ | Fig. 2d | 4 | $12\alpha_A -12\alpha_A^2+4\alpha_A^3$ | $\alpha_B^3$ |
| $f_{12}$ | Fig. 2d | 4 | $4\alpha_A^3$ | $6\alpha_B -4\alpha_B^2+\alpha_B^3$ |
| $f_{22}$ | Fig. 2d | -2 | $4\alpha_A^3-6\alpha_A^2$ | $\alpha_B^3-2\alpha_B^2$ |
| $f_{11}$ | Fig. 2e | 4 | $6\alpha_A -4\alpha_A^2+\alpha_A^3$ | $4\alpha_B^3$ |
| $f_{12}$ | Fig. 2e | 4 | $\alpha_A^3$ | $12\alpha_B -12\alpha_B^2+4\alpha_B^3$ |
| $f_{22}$ | Fig. 2e | -2 | $\alpha_A^3-2\alpha_A^2$ | $4\alpha_B^3-6\alpha_B^2$ |

Table 1: Determination of flexural flexibility matrix coefficients

### 2.2 Shear Sub-Element

The shear sub-element represents hysteretic shear behaviour of the R/C member prior and subsequent to shear cracking, flexural yielding and yielding of the transverse reinforcement. This sub-element has been designed in a similar way to the flexural element described above. It consists of a hysteretic model determining V-γ (shear force vs. shear distortion) behaviour of the member ends and/or intermediate regions and a shear spread-plasticity model determining distribution of shear stiffness along the R/C member.

Shear hysteresis is determined by the V-γ skeleton curve and a set of rules describing response during unloading and reloading. The primary curve is first calculated without considering shear-flexure interaction effect. This initial envelope curve (Fig. 5) is valid for modelling shear behaviour outside the plastic hinge region for members that have yielded in flexure or the response of the entire element for members, where the longitudinal reinforcement remains in the elastic range.

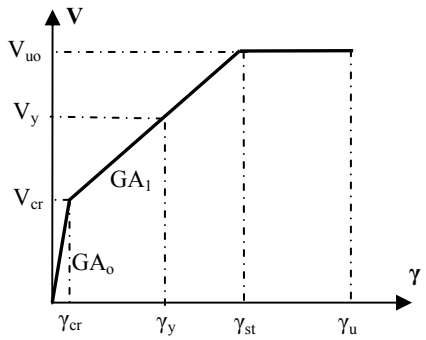


Figure 5: Initial V-γ primary curve

The V-γ initial primary curve consists of four branches (Fig. 5), but only three different slopes, as explained later on. The first branch connects the origin and the shear cracking point, which is defined as the point where the nominal principal tensile stress exceeds the mean tensile strength of concrete [10]. The second and third branches of the initial primary curve have the same slope and connect the shear cracking point to the point corresponding to the onset of yielding of transverse reinforcement, or else the point of attainment of maximum shear strength ($\gamma_{st}$, $V_{uo}$). The second and third branches are separated at the point corresponding to flexural yielding ($\gamma_y$,$V_y$). This approach is adopted in order to distinguish hysteretic shear behaviour before and after flexural yielding.

Shear strength $V_{uo}$ is calculated by the Priestley et al. [11] approach for curvature ductility demand $\mu_\varphi \leq 3$ (i.e. no strength degradation). Shear strain $\gamma_{st}$ is evaluated by the truss analogy approach and two modification factors for the member aspect ratio and normalized axial load, as proposed by the writers of this paper [5,7] on the basis of calibration studies with the experimental evidence.

The fourth branch is almost horizontal and describes shear response after yielding of transverse reinforcement and until onset of shear failure, corresponding to shear distortion $\gamma_u$. On the basis of experimental results coming from 25 R/C specimens failing in shear mode, the writers [5,7] have developed an empirical formula correlating $\gamma_u$ with the level of the applied axial load, the amount of transverse reinforcement and the member shear-span. Conservatively, it is assumed in this study that shear failure coincides with onset of significant lateral strength degradation.

It is well documented [10-12] that shear strength degrades due to disintegration of the plastic hinge zones caused by inelastic flexural deformations. Hence, an R/C member originally

designed with shear capacity higher than the one corresponding to flexural yielding, may eventually experience a brittle shear failure. Additionally, it has been shown experimentally [13,14] that shear distortions in the plastic hinge regions may increase rapidly (shear yielding effect) after flexural yielding, despite the fact that shear force demand remains almost constant as it is controlled by flexural yielding.

The writers have developed a methodology according to which both of these phenomena can be modelled simultaneously and in a rational manner. Following this approach, effective tangent shear stiffness $GA_{eff}$ after flexural yielding is evaluated as a function of $\mu_\varphi$. This stiffness determines modified V-γ envelope curve inside the plastic hinge regions.

Fig. 6 illustrates variation of capacity of shear resisting mechanisms (concrete $V_c$ and truss $V_s$) in the plastic hinge region of a single R/C column following the Priestley et al. [11] shear strength approach (for clarity, contribution of axial load is lumped into $V_c$). It can be seen that after $\mu_\varphi$>3, $V_s$ increases to accommodate both additional shear demand ΔV and additional deterioration of the concrete resisting mechanism $\Delta\text{deg}V_c$.

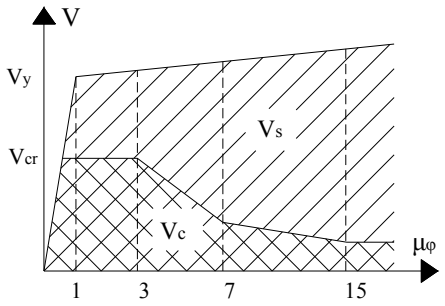


Figure 6: Variation of shear resisting mechanisms with $\mu_\varphi$ in plastic hinges

Generally, after shear cracking, shear strain increment $\Delta\gamma_s$ is related to the additional shear force resisted by the truss mechanism $\Delta V_s$ by Eq. (5), where $GA_1$ is the cracked stiffness of the initial primary curve determined by the truss analogy approach.

$$\Delta\gamma_s = \frac{\Delta V_s}{GA_1} \tag{5}$$

After flexural yielding, $\Delta V_s$ can be considered as the sum of ΔV and $\Delta\text{deg}V_c$. Hence

$$\Delta V_s = \Delta V + \Delta\text{deg}V_c \tag{6}$$

If $GA_{eff}$ is the tangent stiffness of the shear primary curve including shear-flexure interaction effect, it yields the same increment of shear distortions $\Delta\gamma_s$ only for the applied shear force increment ΔV (without $\Delta\text{deg}V_c$), as illustrated in Fig. 7. Consequently

$$\Delta\gamma_s = \frac{\Delta V}{GA_{eff}} \tag{7}$$

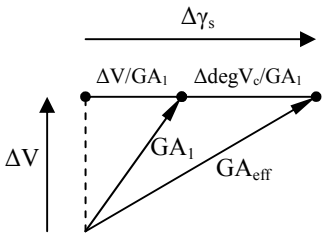


Figure 7: Definition of $GA_{eff}$

By joining Eqs (5-7), Eq. (8) is derived for determining stiffness of the shear envelope curve after yielding in flexure. This formula shows that $GA_{eff}$ can only be either equal or

smaller than $GA_1$. Equality holds only when the degradation of the concrete shear resisting mechanisms is negligible.

$$GA_{eff} = \frac{\Delta V}{\Delta V + \Delta \deg V_c} \cdot GA_1 \tag{8}$$

After determination of the initial and modified V-γ envelope curves, shear hysteretic response has to be established. This behaviour is characterized by significant stiffness degradation and pinching effect. In this study, the empirical model by Ozcebe and Saatcioglu (Fig. 8) is adopted for this response, properly modified by the writers [4] in order to be incorporated in the general inelastic structural analysis framework.

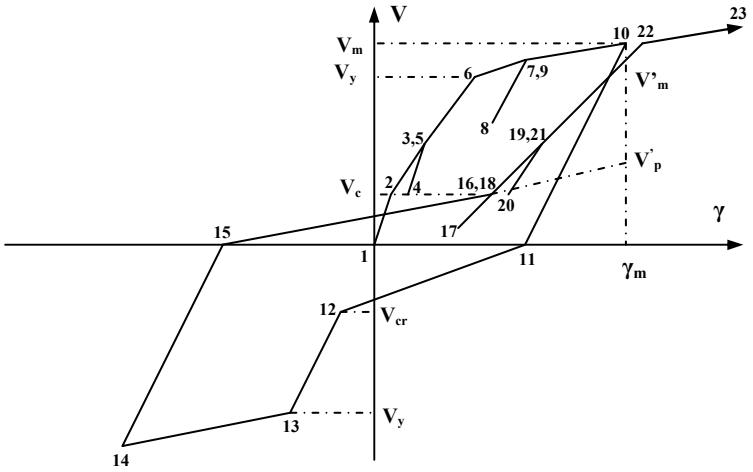


Figure 8: Shear hysteretic model

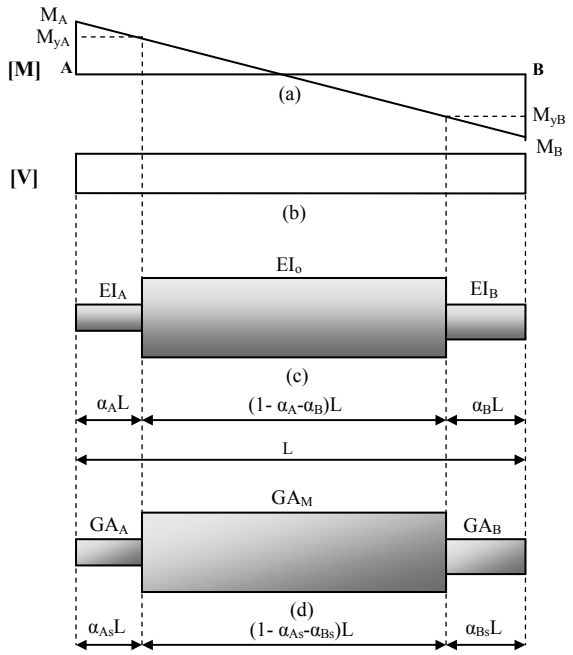


Figure 9: Spread inelasticity models: a) moment diagram; b) shear diagram; c) flexural model; d) shear model

Furthermore, following flexural deformations, inelastic shear strains tend to spread gradually from the ends to the member mid-span as the length of inelastic zones increases. The writers developed a shear gradual spread inelasticity model capable of monitoring variation of

shear stiffness along the concrete member throughout the response. This is achieved by a dual coupling procedure between the flexural and shear sub-element. According to this procedure, the lengths of the inelastic zones $\alpha_{As}$ and $\alpha_{Bs}$ of the shear sub-element are defined by the respective ones of the flexural sub-element (Fig. 9). In addition, the stiffness of these zones $GA_A$ and $GA_B$ are determined by the modified V-γ envelope curves calculated for the curvature ductility demands of the respective ends of the flexural member model. Shear stiffness $GA_M$ of the intermediate part of the member is determined by the initial V-γ primary curve, without considering shear-flexure interaction effect.

After determining the distribution of *GA* along the R/C member at each step of the analysis, the coefficients of the flexibility matrix of the shear sub-element are given by Eq. (9).

$$f_{ij}^{sh} = \frac{a_{As}}{GA_A \cdot L} + \frac{1 - a_{As} - a_{Bs}}{GA_M \cdot L} + \frac{a_{Bs}}{GA_B \cdot L} \quad \text{(i,j=1,2)} \tag{9}$$

### 2.3 Bond-Slip Sub-Element

The bond-slip sub-element accounts for the fixed-end rotations ($\theta_{slip}$) which arise at the interfaces of adjacent R/C members due to bond deterioration and slippage of the reinforcement in the joint regions. The proposed model consists of two concentrated rotational springs located at the member-ends. The two (uncoupled) springs are connected by an infinitely rigid bar (Fig. 1e). Following this formulation, the coefficients of the bond-slip flexibility matrix $F^{sl}$ are given simply by Eq. (10), where $f_A^{sl}$ and $f_B^{sl}$ are the flexibilities of the concentrated rotational springs at the ends A and B respectively. These flexibilities depend on the envelope curve and the model used to represent hysteretic behaviour of each rotational spring.

$$F^{sl} = \begin{bmatrix} f_A^{sl} & 0 \\ 0 & f_B^{sl} \end{bmatrix} \tag{10}$$

The M-$\theta_{slip}$ skeleton curve is derived on the basis of a simplified procedure [15,16] assuming uniform bond stress along different segments of the anchored rebar (Fig. 10). These segments are the elastic region $L_e$, the strain strain-hardening region $L_{sh}$ and the cone penetration zone $L_{pc}$. The average elastic bond strength $\tau_{be}$ of ACI 408 [17] is adopted here for the elastic region, while the frictional bond $\tau_{bf}$ of the C.E.B. Model Code [18] is assumed to apply within the strain-hardening region. In the cone penetration zone, it is assumed that the acting bond is negligible.

For various levels of the applied end moment and using the results of the M-φ analysis, the stress $\sigma_s$ and strain $\varepsilon_s$ of the reinforcing bar at the loaded end are first determined. Then, by equilibrium and applying the assumed bond distribution, variation of reinforcing bar stress $\sigma_s(x)$ along the embedment length is defined as shown in Fig. 10a, where $\sigma_y$ is the yield strength of steel and $\sigma_h$ is the stress at the end of the straight part of the rebar anchorage. Later, by assigning an appropriate constitutive material law [19], strain distribution $\varepsilon_s(x)$ is determined, as shown in Fig. 10b, where $\varepsilon_y$ and $\varepsilon_{sh}$ are the steel strains at the onset of yielding and strain hardening and $\varepsilon_h$ is the steel strain at the end of the straight part of the anchorage. It is important to note that nonlinearity of strain hardening material law should be taken into account because it influences significantly the final results [5].

Once $\varepsilon_s(x)$ is determined, slip of the reinforcement $\delta_{slip}$ can be calculated by integration along the anchored length of the bar. In the case of hooked bars, local slip of the hook should be added. This can be evaluated by the force acting on the hook $P_h=A_b \cdot \sigma_h$, where $A_b$ is the area of the anchored bar, and an appropriate hook force-hook slip relationship [20].

Upon determination of $\delta_{slip}$, the respective fixed-end rotation can be calculated by Eq. (11), where $(d-x_c)$ is the distance between the bar and the neutral axis.

$$\theta_{slip} = \frac{\delta_{slip}}{d - x_c} \tag{11}$$

The envelope M-$\theta_{slip}$ curve constructed by the various points of the afore-described methodology is then idealized by a bilinear relationship for the purposes of analysis.

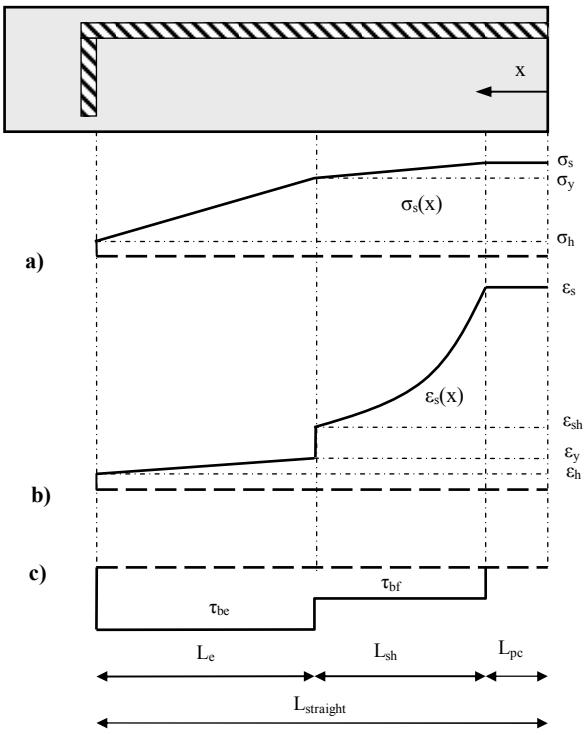


Figure 10: Reinforcing bar with 90° hook embedded in concrete; a) stress distribution; b) strain distribution; c) bond distribution.

In R/C structures with substandard detailing, anchorage-bond failures cannot be precluded. In case of straight anchorages, bond failure takes place when the anchorage length demand $L_{dem}$ reaches the available straight embedment length $L_{straight}$. This occurs for $\sigma_s>\sigma_y$, when Eq. (12) holds, where $d_b$ represents bar diameter. If $\sigma_s$ exceeds the one corresponding to flexural failure, then bond is not the critical mode of failure for the examined anchorage.

$$\sigma_s = \sigma_y + \frac{4 \cdot \tau_{bf}}{d_b} \cdot \left( L_{straight} - L_{pc} - \frac{\sigma_y \cdot d_b}{4 \cdot \tau_{be}} \right) \tag{12}$$

For very short embedment lengths, where bond failure takes place for $\sigma_s<\sigma_y$, experimental evidence [17] shows that the assumption of uniform bond strength $\tau_{be}$ underestimates significantly the available anchorage capacity. To avoid over-conservative solutions, it is assumed in this study that actual available bond force $T_d$ is derived from linear interpolation between the capacity bond forces corresponding to two well documented available anchorage bond lengths (Fig. 11). The first bond strength $T_{d1}$ refers to $L_{straight}=5d_b$, where the ultimate bond stress $\tau_{bu}$ of the local bond-slip constitutive law (C.E.B. Model Code [18]) is assumed to develop uniformly. Thus

$$T_{d1} = 5 \cdot d_b \cdot u \cdot \tau_{bu} \tag{13}$$

Where, u is the bar perimeter. The second bond strength $T_{d2}=A_b\cdot\sigma_y$ refers to $L_{straight}=l_d$, where $l_d$ is the development length (Eq. 14) corresponding to yielding of the reinforcement. Along this length, uniform bond strength $\tau_{be}$ is considered.

$$l_d = \frac{\sigma_y \cdot d_b}{4 \cdot \tau_{be}} \tag{14}$$

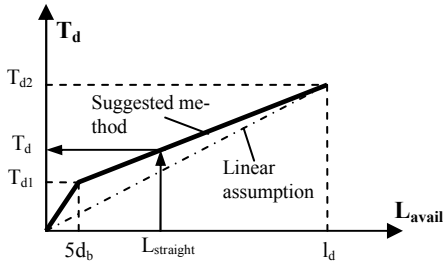


Figure 11: Determination of available straight anchorage bond strength for very short embedment lengths

In the case of deficient end hooks, anchorage failure may be assumed to develop, when the force acting on the hook reaches ultimate hook capacity $P_{hu}$. Depending on the range of $\sigma_s$ and the available straight anchorage length $L_{straight}$, Eq. (15) holds for determining $\sigma_s$, where $L_{sh}=(\sigma_s-\sigma_y)\cdot d_b/(4\cdot\tau_{bf})$ for $\sigma_s>\sigma_y$.

$$\sigma_s = \frac{P_{hu} + \pi \cdot d_b \cdot \tau_{be} \cdot L_{straight}}{A_{sb}} \quad \text{for } \sigma_s \le \sigma_y$$

$$\sigma_s = \sigma_y + \frac{4 \cdot \tau_{bf}}{d_b} \cdot \left( L_{straight} - L_{pc} - \frac{\left(A_{sb} \cdot \sigma_y - P_{hu}\right)}{\pi \cdot d_b \cdot \tau_{be}} \right) \quad \text{for } \sigma_s > \sigma_y \text{ and } L_{straight}-L_{pc}-L_{sh}>0 \tag{15}$$

$$\sigma_s = \frac{P_{hu} + \pi \cdot d_b \cdot \tau_{bf} \cdot \left(L_{straight} - L_{pc}\right)}{A_{sb}} \quad \text{for } \sigma_s > \sigma_y \text{ and } L_{straight}-L_{pc}-L_{sh}<0$$

After determining M-$\theta_{slip}$ bilinear skeleton curve, bond-slip hysteretic behaviour (Fig. 12) is modelled following the suggestions of Saatcioglu and Alsiwat [21].

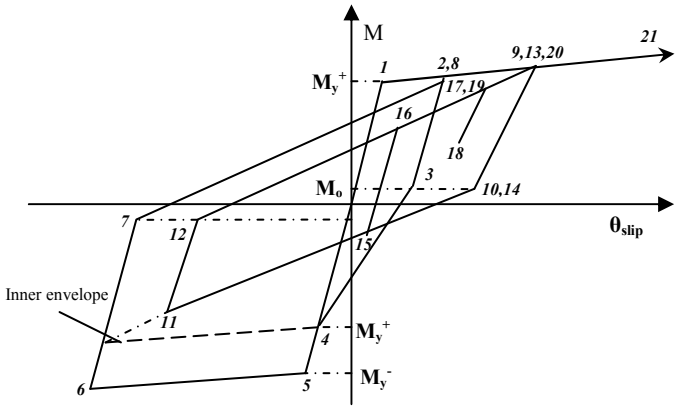


Figure 12: M-$\theta_{slip}$ hysteretic model.

## 3 NUMERICAL IMPLEMENTATION

The finite element model, described above, requires additional modifications to the nonlinear analysis solution algorithms in order to be implemented with consistency. It is known that during nonlinear analysis the following equation is solved in incremental form.

$$K\cdot\Delta U=\Delta F \tag{16}$$

Where K is the overall tangent stiffness matrix of the structure, $\Delta U$ is the vector of unknown nodal displacement increments and $\Delta F$ is the vector of the applied external load in-

crements. The element stiffness matrices $K_e$ are first calculated at the element level and later assembled into K**.**

In the case of dynamic analysis, the equivalent dynamic stiffness and external load matrices must be formed [22]. The solution of the incremental system is carried out using the unconditionally stable constant-average acceleration Newmark-Beta algorithm [23]. Viscous damping matrix is calculated by assigning the Rayleigh damping model with circular frequencies corresponding to the first and second mode of vibration.

The solution is performed assuming that the properties of the structure do not change during the analysis step. Since the stiffness of some elements is likely to change during the step t, the new configuration at t+Δt may not satisfy equilibrium. If $\Delta F_{ln}$ is the force increment vector arising from the assumption of constant stiffness during Δt and $\Delta F_{nl}$ is the force increment vector determined by the element nonlinear hysteretic laws, then an unbalanced force vector $\Delta F_{ub}$ arises, given by the following equation

$$\Delta F_{ub} = \Delta F_{ln} - \Delta F_{nl} \tag{17}$$

Typically, in the nonlinear analysis scheme, this issue is resolved by applying the one step unbalanced force correction method [22,24]. According to this technique, the unbalanced force vector is subtracted from the right part of Eq. (16) at the next time step of analysis. Despite the fact that this procedure minimizes computational effort in nonlinear analysis, it cannot be applied with consistency for finite elements composed by different sub-elements connected in series.

Fig. (13) presents determination of unbalanced forces produced by two different hysteretic laws (F-$v_1$ and F-$v_2$), which are connected in series. The two hysteretic relationships have different elastic ($k_{T1}$ and $k_{T2}$) and post-elastic stiffness ($r_1 \cdot k_{T1}$ and $r_2 \cdot k_{T2}$). It can be easily extracted that for the same force increment $\Delta F_{ln}$ the restoring force increments $\Delta F_{nl1}$ and $\Delta F_{nl2}$ and consequently unbalanced forces $\Delta F_{ub1}$ and $\Delta F_{ub2}$ become different, resulting in loss of member equilibrium.

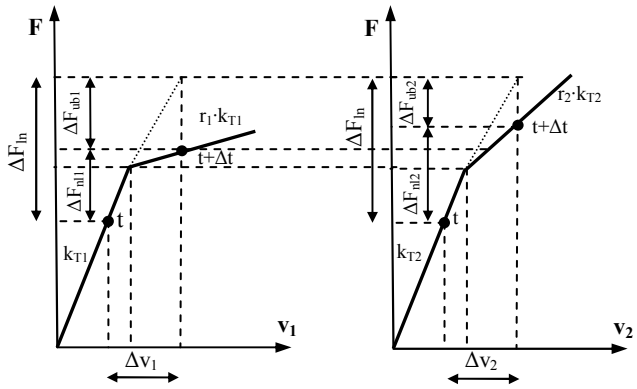


Figure 13: Unbalanced forces for two hysteretic relationships connected in series

To overcome this problem, the 'event to event' solution strategy [25] is adopted herein. This method is enhanced to cope with the finite element model proposed in this study. In accordance with this procedure, the nonlinear response of the structure is subdivided into subsequent events, which mark the change of stiffness of the entire structure. Between these events, linear behaviour is considered. To achieve this goal, each step is divided (when required) into sufficient number of sub-steps, until no event takes place during the last sub-step. For the finite element developed herein, as an event is prescribed every change in stiffness of all hysteretic responses of all three sub-elements of each beam-column model.

If the incremental load vector ΔF yields the deformation increment $\Delta v_{mn}$ for the hysteretic response n of the element m, assuming constant stiffness, then the next event e force scale factor $\lambda_{mn}$ corresponding to this hysteretic response is determined by

$$\lambda_{mn} = \min\left(1, \frac{v_{mne} - v_{mn}}{\Delta v_{mn}}\right) \tag{18}$$

In Eq. (18), $v_{mne}$ is the deformation marking this event and $v_{mn}$ is the same deformation at the beginning of the loading step. It is obvious, that the immediate next event for the entire structure will correspond to the minimum value $\lambda_{min}$ of all $\lambda_{mn}$. After calculating $\lambda_{min}$, the solution algorithm implemented to each nonlinear analysis step is presented in Fig. 14.

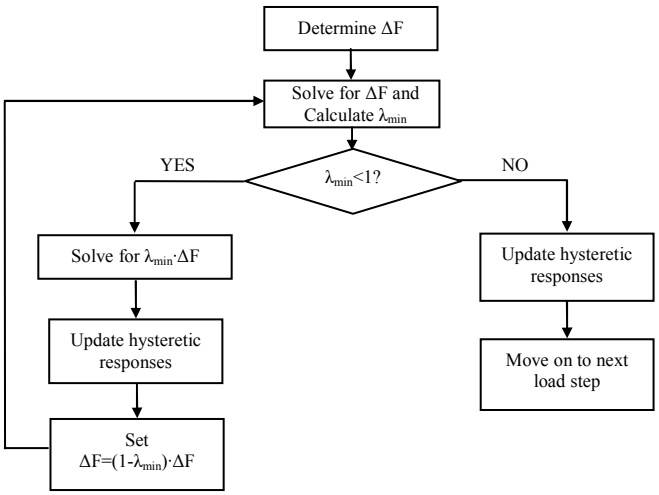


Figure 14: Event to event solution algorithm

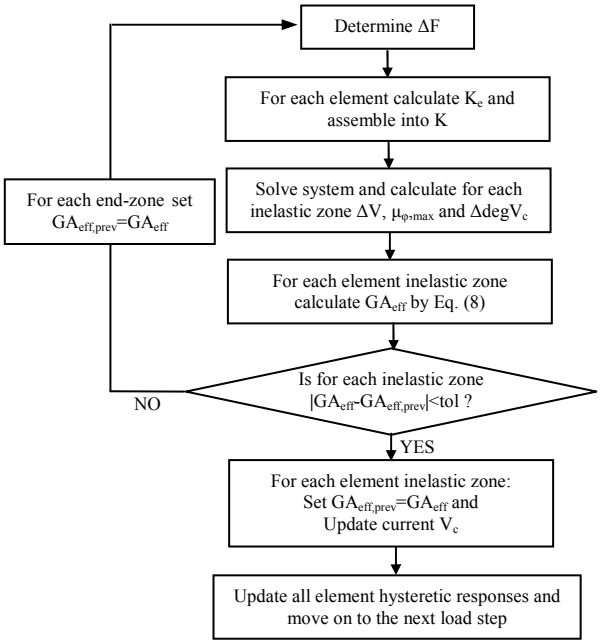


Figure 15: Shear-flexure interaction implementation algorithm

Additionally, following the procedure adopted in this study for determining tangent shear stiffness $GA_{eff}$ after flexural yielding when accounting for shear-flexure interaction effect, it is evident from Eq. (8), that $GA_{eff}$ becomes a function of the element shear force increment ΔV.

But if it is to be applied in the analytical procedure, $\Delta V$ will be influenced by $GA_{eff}$ as well, since the latter will affect the flexibility matrix of the element, as given by Eqs. (1) and (9). To resolve this issue, an iterative analytical scheme, applied in the respective load step of the nonlinear analysis, is proposed herein, as detailed in the algorithm shown in Fig. 15.

Applying this procedure, it was found that numerical convergence is almost immediate. The number of iterations may increase as the influence of shear deformations on element flexibility enhances, but the additional computational cost required is justified by the significance of calculating accurately shear response in this case.

## 4 VALIDATION OF THE PROPOSED MODEL

The numerical model described above is implemented in the general finite element code IDARC2D developed at the State University of New York at Buffalo [22]. Then, it is validated against experimental results coming from three well documented R/C frame specimens with substandard detailing.

In addition, parametric analyses reveal the necessity of incorporating each deformation mechanism in seismic assessment of 'old type' R/C structures in the linear and nonlinear range of response. To this puropose, each frame specimen is examined using four different beam-column models. The F model simulates only member flexural response. The FB model incorporates flexural and anchorage bond-slip response, while the FS one applies flexural and shear flexibility. Finally, the FSB model, which is the one proposed in this study, simulates all deformation mechanisms, as well as their interaction.

### 4.1 Frame specimen Duong et al. (2007) [26]

A single-span, two-storey, shear critical R/C frame with a fixed base condition was constructed and tested in the facilities at University of Toronto. This test frame was 2:3 in scale and stood approximately 4.6m tall and 2.3m wide. Beams and columns had dimensions 300mmX400mm. Frame reinforcement layout is depicted in Fig. 16 as well as cross-sections detailing. The average concrete compressive strength at the time of the test was 43MPa. No. 10, No. 20 and US No. 3 were used in the specimen, with yield strengths of 455, 447 and 506MPa respectively. Further information regarding material characteristics can be found in [26].

An axial load of 420kN was applied to the top of each column and maintained in a force-controlled manner. Lateral action was applied only at the top level of the frame. Initially, the specimen was subjected to a forward lateral drift of about 1.0% (44mm) by which point significant shear damage had occurred in the beam of the first storey and failure appeared imminent. Then, the specimen was unloaded and afterwards a reverse load was applied until the frame reached the same displacement as in forward cycle. Finally, the specimen was again unloaded until approximately zero lateral force.

Fig. 17 presents the analytical finite element model used for the analysis of the frame under examination. It solely consists of six beam column elements assuring high computational efficiency. Frame joints are modelled via rigid arms at the ends of each member. Columns are assumed to be fixed into the foundation beam.

Initially and in order to investigate specimen capacity, pushover analyses are conducted for all finite element model types (F, FB, FS, FSB). Fig. 18 illustrates the lateral force-lateral top displacement curves obtained. It is clear that considering only flexural deformations leads to significant overestimation of frame stiffness, strength and displacement capacity. Incorporating fixed end rotations arising from anchorage bond-slip in model FB, reduces substantially

the predicted initial frame stiffness. However, since no shear failure can be predicted, displacement capacity is grossly overestimated. Ultimate lateral strength capacity almost reaches the respective one coming from the F model. The FS analytical model predicts adequately initial frame stiffness. Nevertheless, since fixed-end rotations are not included, the model underestimates the level of lateral displacement at which shear failure is initiated (35mm instead of 44.7mm).

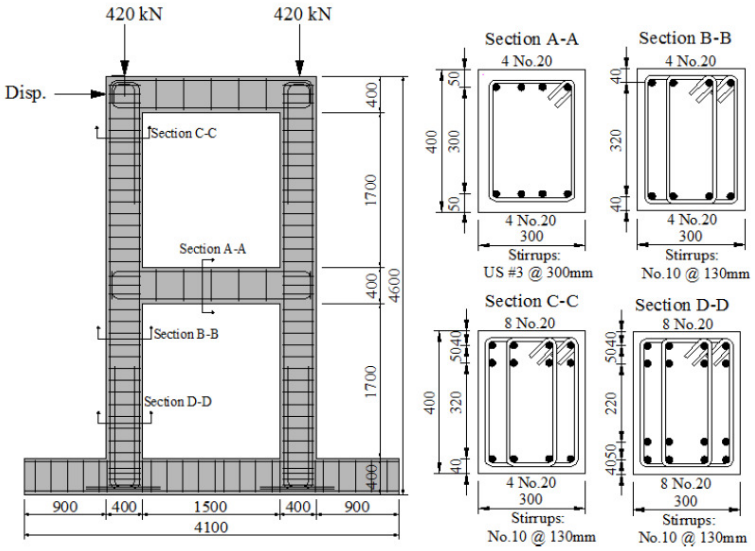


Figure 16: Duong et al. (2007) frame reinforcement layout and cross-section detailing

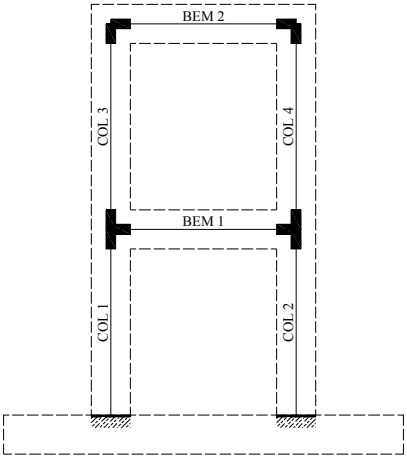


Figure 17: Duong et al. (2007) frame finite element model

The complete FSB model follows closely experimental response. Very small underestimation of initial stiffness may be attributed to the fact that the flexural pre-cracking response is not modelled in this study. The analytical model predicts accurately the lateral displacement corresponding to onset of shear failure (45mm instead of 44.7mm). Lateral strength capacity is slightly overestimated (about 10%).

For the same model, if degradation of shear strength with flexural demand is neglected, then displacement capacity becomes 159mm. On the contrary, if shear strength is assumed from the beginning of the analysis equal to its minimum value (corresponding to $\mu_\varphi \geq 15$), then displacement capacity drops to 10mm. It is recalled that the latter approach is the one adopted by modern seismic codes.

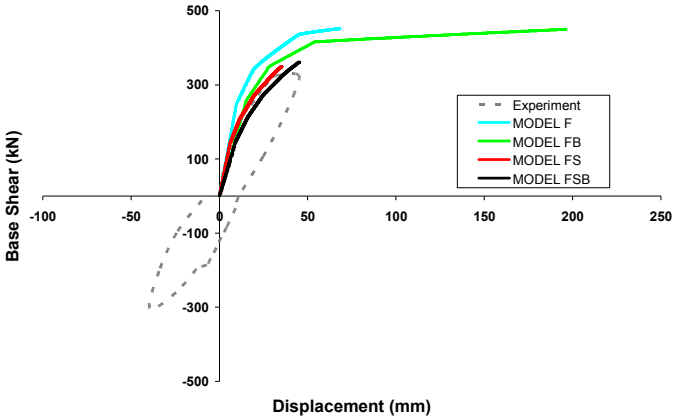


Figure 18: Pushover curves for Duong et al. (2007) frame specimen

Fig. 19 illustrates the modes of failure predicted by all analytical models at the end of pushover analysis. It is shown that while the models including inelastic shear effect (FS and FSB) predict the experimental mode of failure, which is the development of shear failure at the first-storey beam after flexural yielding, the other two models foresee erroneously a flexural failure of the same beam.

Fig. 20 compares the experimental and analytical base shear vs. top displacement response derived by the analytical models F, FB and FSB. As explained before, FS model predicted a premature shear failure and analysis had to stop prior to unloading response. It can be seen that the FSB analytical model correlates well with the experimental evidence in the whole range of response. Residual displacement after first unloading is estimated 13.5mm instead of 10.8mm. At the end of loading in the negative direction lateral frame strength is again slightly overestimated (approx. 10%). During unloading in the negative direction, initial frame stiffness is underestimated, but as an average in the whole unloading range stiffness is calculated satisfactorily. Hence, residual displacement after second unloading is found equal to 10.5mm opposed to 7.5mm. The analytical models F, FB overestimate significantly frame lateral stiffness and strength yielding higher estimates regarding total energy dissipated by the specific specimen.

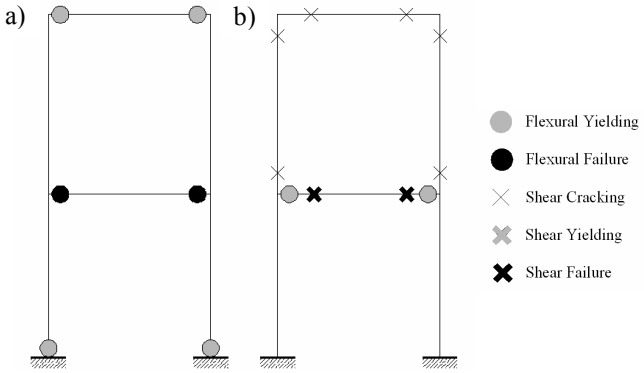


Figure 19: Predicted modes of failure for Duong et al. (2007) frame specimen by pushover analysis with a) F and FB; b) FS and FSB analytical model.

The hysteretic responses of the shear critical first storey beam produced by the FSB analytical model are presented in Fig. 21. Only one end-section is shown, since anti-symmetric response was predicted for this member. It can be inferred by this figure that the specific end-section yields first in positive bending developing high curvature ductility demand. Due to shear-flexure interaction effect, shear strains inside plastic hinge increase more rapidly than

outside plastic hinge region. This increase is followed by yielding of the transverse reinforcement, which differentiates substantially shear response inside and outside the inelastic region. At peak response, maximum shear strain is 1.8% and 0.7% in the yielded and non-yielded part of the member respectively. In the negative direction, the analytical model does not predict yielding of the transverse reinforcement, as observed experimentally. This is due to the fact that $\mu_\varphi$ demand is not calculated to be higher than 3 and shear-flexure interaction effect is not triggered according to [11]. Hence, shear strains inside and outside plastic hinge region are estimated to be equal.

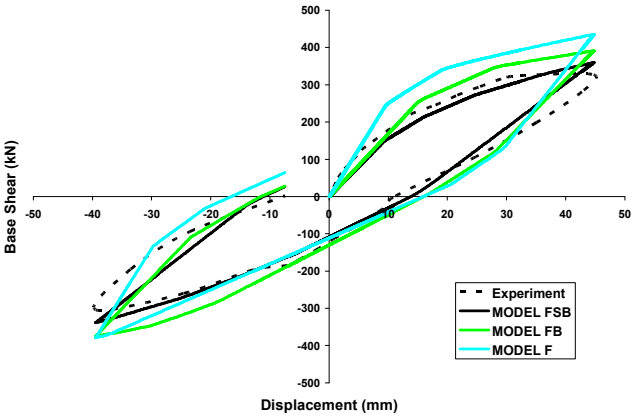


Figure 20: Pushover curves for Duong et al. (2007) frame specimen

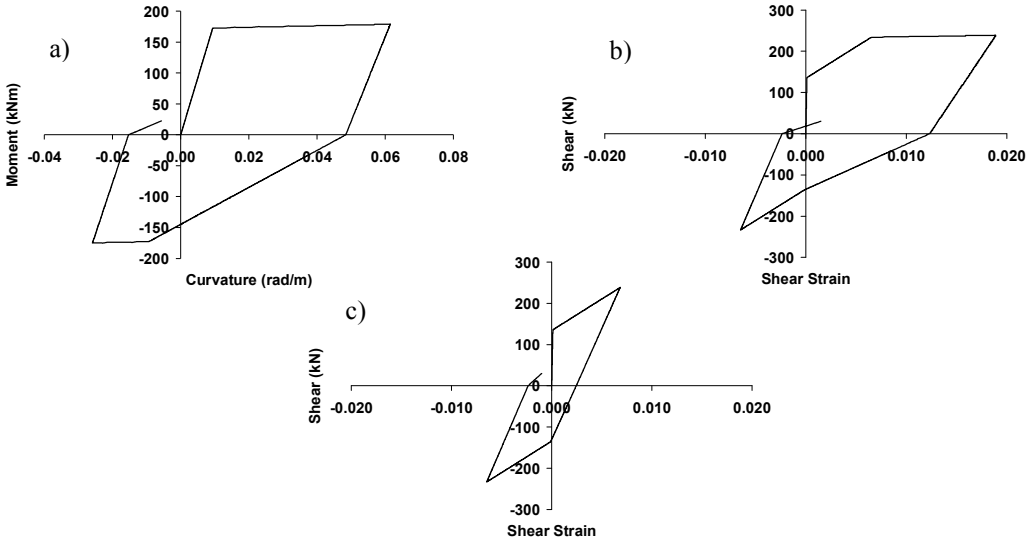


Figure 21: Duong et al. (2009) first storey beam hysteretic responses a) end-section M-φ; b) V-γ inside plastic hinge region; c) V-γ outside plastic hinge region.

### 4.2 Frame specimen 1 by Elwood & Moehle (2008) [27]

The specific half-scale specimen was constructed and tested on the shaking table at the University of California, Berkeley. It comprised three columns interconnected at the top by a 1.5m wide beam and supported at the bottom on footings (Fig. 22). The columns supported a total mass of 31t. To represent R/C columns typical of 1960s construction in the western United States, the central column was constructed with light transverse reinforcement having $90^o$ hooks (Fig. 22). The outside columns were detailed with closely spaced spiral reinforcement to ensure ductile response and to provide support for gravity loads after shear failure of the central column. The specimen was subjected to one horizontal component of the ground

motion recorded at Viña del Mar during the 1985 Chile earthquake (SE32 component). The normalized central column axial load was 0.10. During testing, the central column of specimen 1 experienced a loss of lateral load capacity, apparently due to shear failure [27]. In Fig. 23, the finite element model applied for this analytical study is depicted. Its simplicity secures maximum computational efficiency. In the following, shear strength coming from transverse reinforcement of the central column is reduced to the half due to its deficient anchorage.

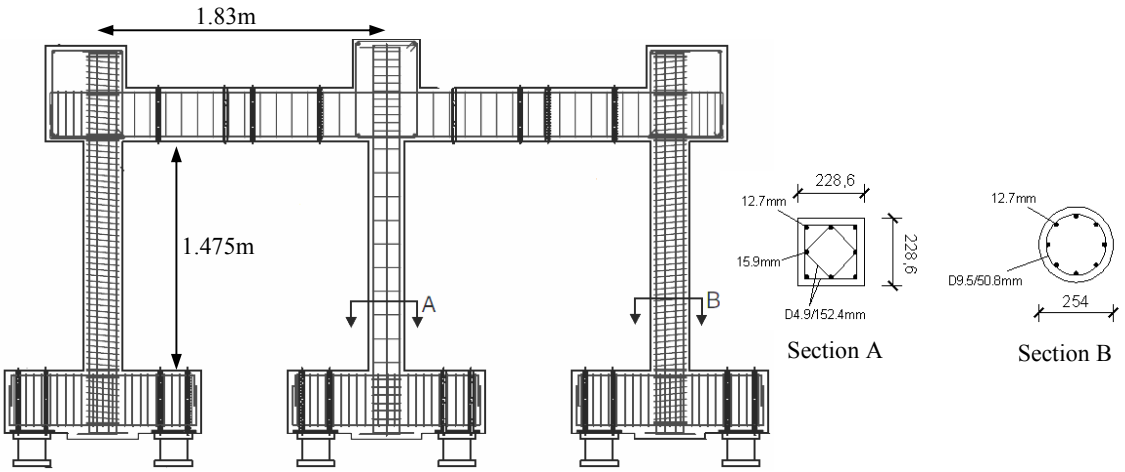


Figure 22: Elwood & Moehle (2008) frame reinforcement layout and cross-section detailing

Initially, modal response analyses were conducted including all four finite element models. Table 1 summarizes the vibration periods T estimated. The smallest period comes from the stiffest F model, which ignores shear and bond flexibility. Anchorage slip lengthens significantly the vibration period from 0.28sec to 0.33sec. On the contrary, shear deformations have minor effect on T. This is because of the fact that at this analysis stage uncracked shear stiffness is employed in the analytical model. The models FB and FSB predict well the experimental value of T ranging between 0.30sec and 0.35sec.

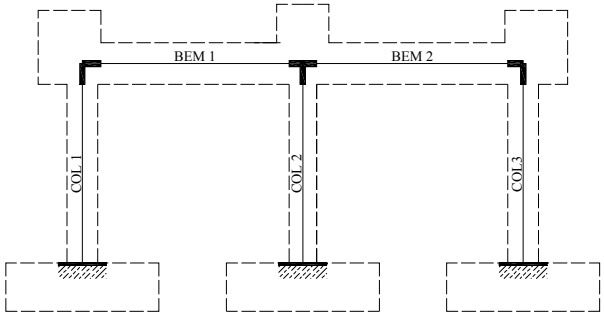


Figure 23: Elwood & Moehle (2008) frame finite element model

| Model | F | FB | FS | FSB |
|---|---|---|---|---|
| T (sec) | 0.283 | 0.333 | 0.285 | 0.335 |

Table 2: Elwood & Moehle (2008) frame predicted vibration periods

Fig. 24 presents base shear ($V_{base}$) vs. top displacement ($\Delta_{top}$) relationships attained by pushover analysis of this frame as well as the experimental response recorded in the positive direction of loading. It can be seen that the F analytical model overestimates considerably initial lateral stiffness and undervalues very importantly displacement corresponding to onset of lateral failure. Inclusion of anchorage slip leads to sufficient prediction of initial stiffness until a value of $V_{base}\approx$150kN. After this level, the analytical model fails to follow closely gradual

degradation of lateral stiffness and predicts a displacement capacity value of 38mm. The FS model prediction lies between the two aforementioned analytical curves. Lateral displacement capacity is found 29mm in this case. The FSB analytical model prediction converges adequately the experimental envelope for almost the entire range of response. Lateral displacement capacity is estimated equal to 46mm, which is in relatively good agreement with the experimental observation (approx. 55mm).

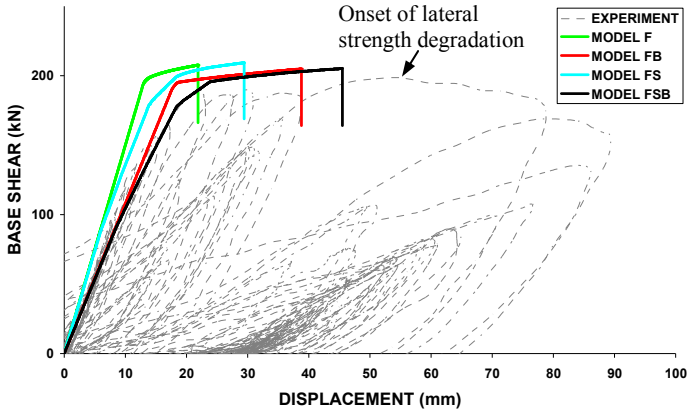


Figure 24: Elwood & Moehle (2008) frame predicted pushover curves

Fig. 25 illustrates the critical modes of failure as foreseen by the four analytical models. It is shown that the models not incorporating shear effect predict erroneously the development of flexural type of failure at the base of the central column. On the contrary, the FS and FSB analytical models drive to the experimentally observed final damage state composed by a shear failure at the top of the central column following flexural yielding.

Closing with pushover analysis, it is important to mention that if degradation of shear strength with flexural demand is neglected, the FSB analytical model predicts erroneously a flexural failure at the base of the central column for lateral displacement equal to 48mm. On the other hand, if shear strength is assumed from the beginning of the analysis equal to its minimum value (corresponding to $\mu_\varphi \geq 15$), then a shear failure is predicted corresponding to a displacement demand of only 17mm.

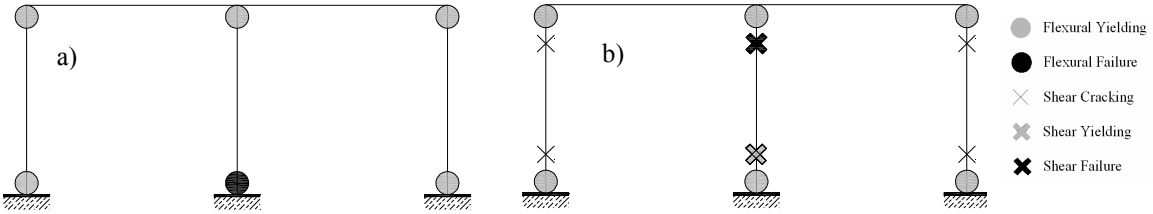


Figure 25: Predicted modes of failure for Elwood & Moehle (2008) frame specimen by pushover analysis with a) F and FB; b) FS and FSB analytical model.

Fig. 26 compares the experimental recordings and the analytical predictions produced by the proposed FSB finite element model, when the examined specimen is subjected to the ground motion component. For the analysis purposes, time step is chosen to be 0.005sec and viscous damping coefficient equal to 1% of its critical value. It can be seen that the analytical model estimates very well the displacement and base shear time histories for the major part of the response. Deviations from the experimental measurements are observed between 18.6sec and 23.1sec and between 26.0sec and 28.6sec. These time periods follow sharp excursions during which yielding of transverse reinforcement has been observed. The deviations may be

attributed to the fact that the proposed finite element cannot model, in its present form, degradation of shear strength after yielding of the transverse reinforcement, as observed experimentally.

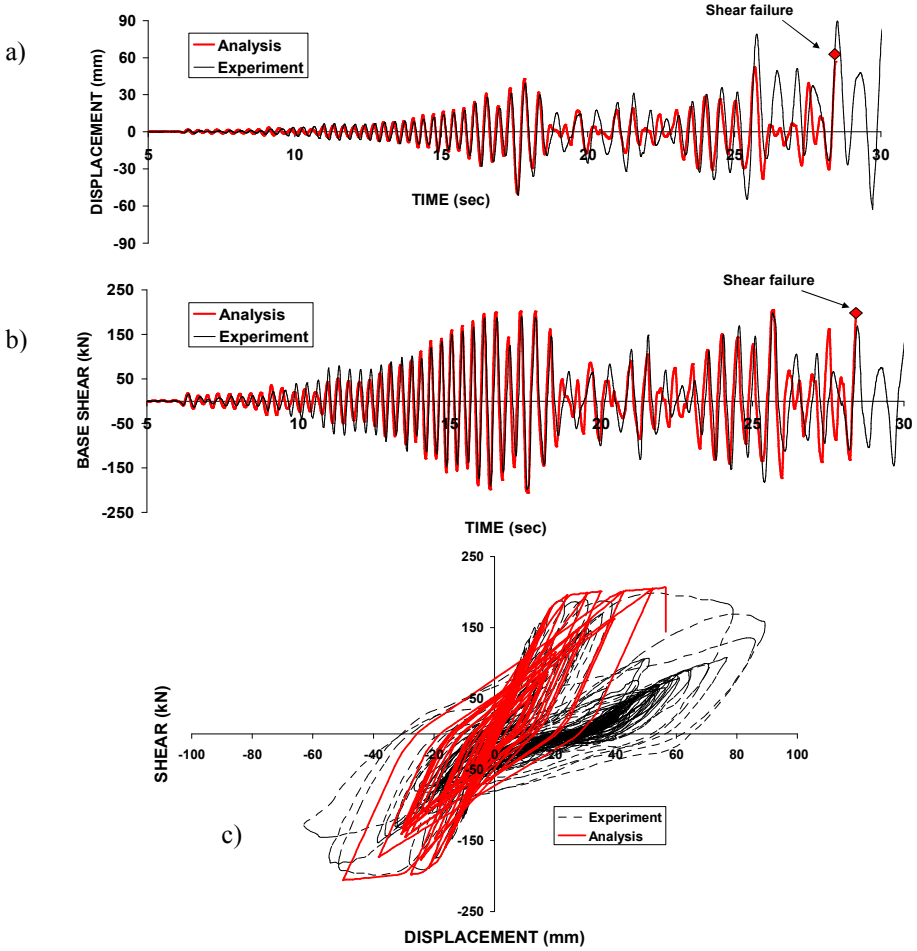


Figure 26: Elwood & Moehle (2008) frame specimen responses as recorded experimentally and predicted by FSB analytical model. a) lateral displacement time history; b) base shear time history; c) $V_{base}$ vs. $\Delta_{top}$ response.

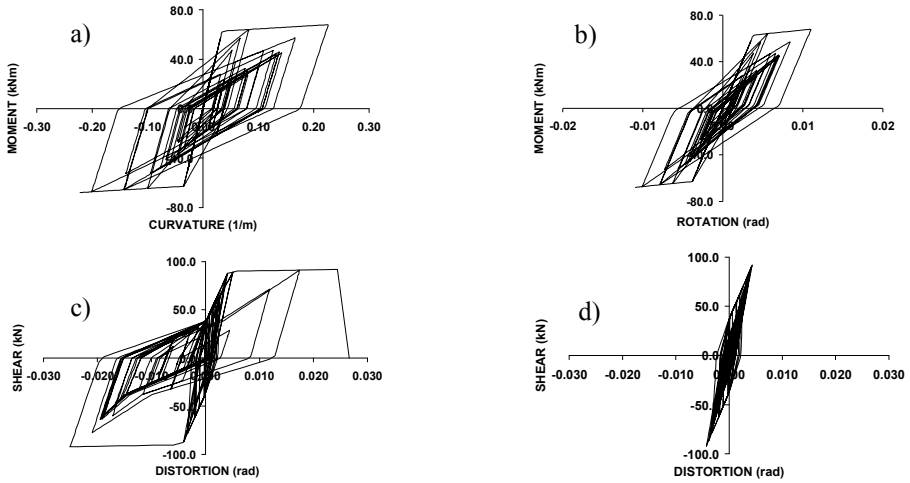


Figure 27: Elwood & Moehle (2008) central column predicted hysteretic responses. a) M-φ at the top; b) M-$\theta_{slip}$ at the top; c) V-γ at the top plastic hinge; d) V-γ outside plastic hinges

Fig. 26c compares the experimental and analytical $V_{base}$-$\Delta_{top}$ hysteretic relationships. It is evident that the proposed model captures sufficiently initial (elastic) stiffness, strength capacity as well as unloading and reloading response up to onset of lateral strength degradation. It must be emphasized that nonlinear dynamic analysis using the FSB model estimates accurately the magnitude of displacement corresponding to onset of shear failure and consequent lateral strength degradation, while pushover analysis yields approximately 17% underestimation of the specific response.

Fig. 27 presents hysteretic responses of the central shear-critical column, as derived by the analytical model. It can be seen that flexural yielding has been predicted at the top of the specific column followed by significant hysteretic response in flexure and anchorage slip. Due to inelastic flexural deformations, shear strength degrades in the plastic hinge of the member. Based on the shear-flexure interaction procedure proposed in this study, shear strains increase more rapidly inside than outside the inelastic zone. This phenomenon is accompanied by yielding of transverse reinforcement in the plastic hinge region driving to further differentiation of shear strains in the two discrete regions.

Finally, it is worth reporting that the predicted damage state of the examined frame from inelastic dynamic analysis is the same with the one shown in Fig. 25b, in agreement with the experimental evidence.

### 4.3 Frame specimen El-Attar et al. (1997) [28]

A 1/6 scale 2-storey one-bay by one-bay lightly reinforced concrete building was tested on the Cornell University shake table. The structure was designed solely for gravity loads, without regard to any kind of lateral loads. The reinforcement details (Fig. 28) were based on typical R/C frame structures constructed in the Central and Eastern United States since the mid 1900's. Model structure concrete strength was 32.3MPa (4.7ksi) and steel reinforcement yield capacity 414MPa (60ksi).

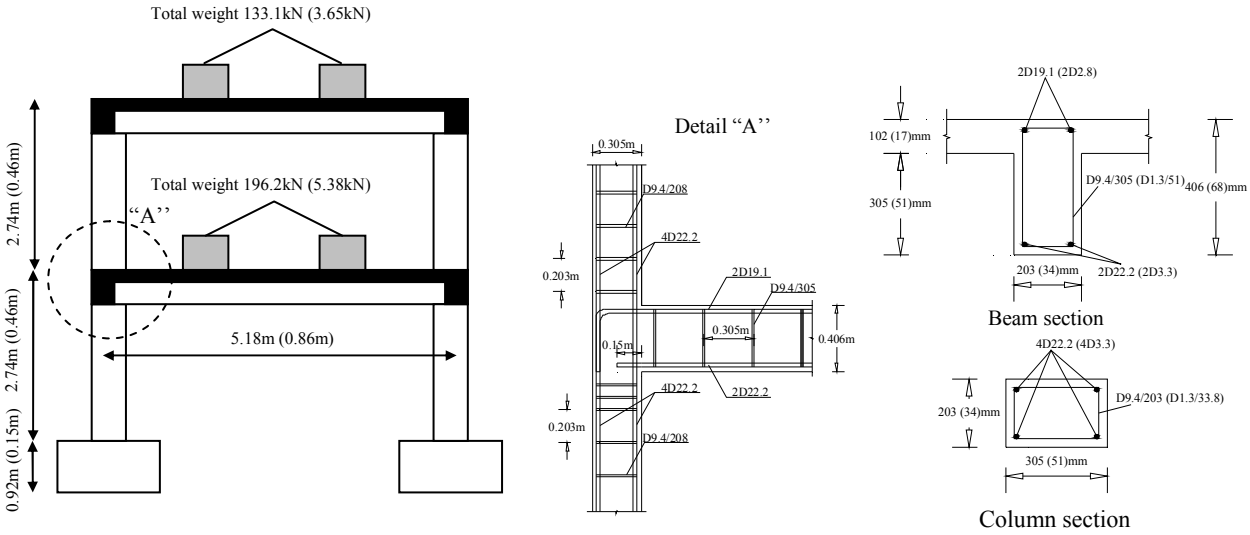


Figure 28: El-Attar et al. (1997) frame specimen configuration (values outside and inside parentheses correspond to prototype and model structure respectively).

The model structure was tested using the time-scaled Taft 1952 S69E earthquake with peak ground acceleration set in increasingly higher values. After running Taft 0.45g, wide, deep

cracks were observed in the beams around the locations of discontinuous positive beam reinforcement (at the joint panels), indicating bond failure and pending pullout of these bars [28].

Fig. 29 compares frame response histories derived by the FSB analytical model and experimental recordings for the 0.36g peak ground acceleration. It is evident that the proposed model follows closely the experimental response after the first 1.5sec. Small differentiations are justifiable considering the large scale (1/6) of the examined specimen.

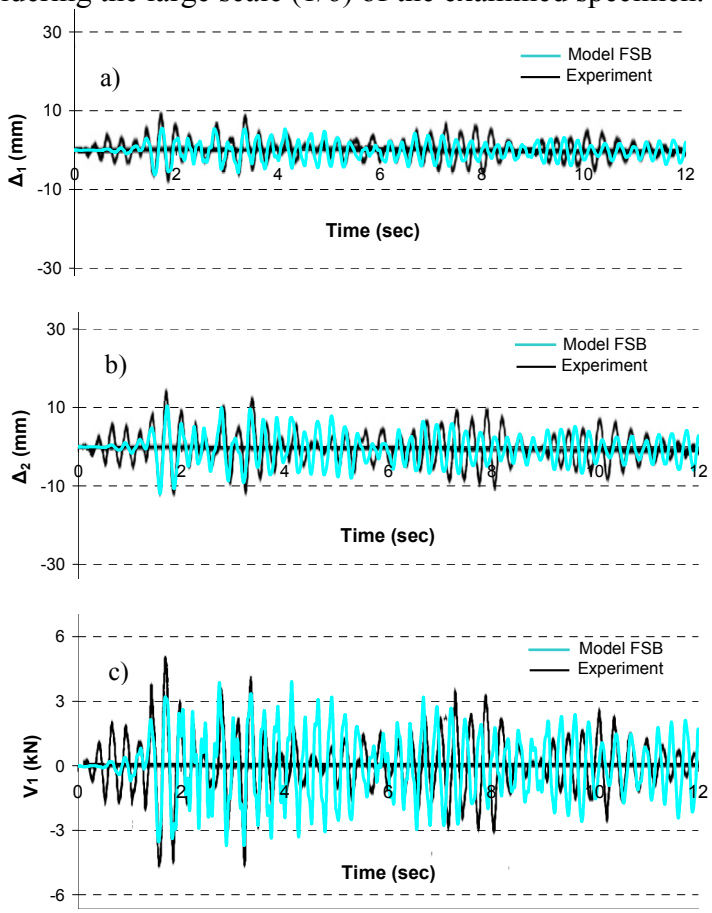


Figure 29: Comparison of El-Attar et al. (1997) frame specimen time history responses from the experimental recordings and analytical model FSB for Taft 0.36g acceleration record: a) 1st storey total displacement; b) 2nd storey total displacement; c) base shear

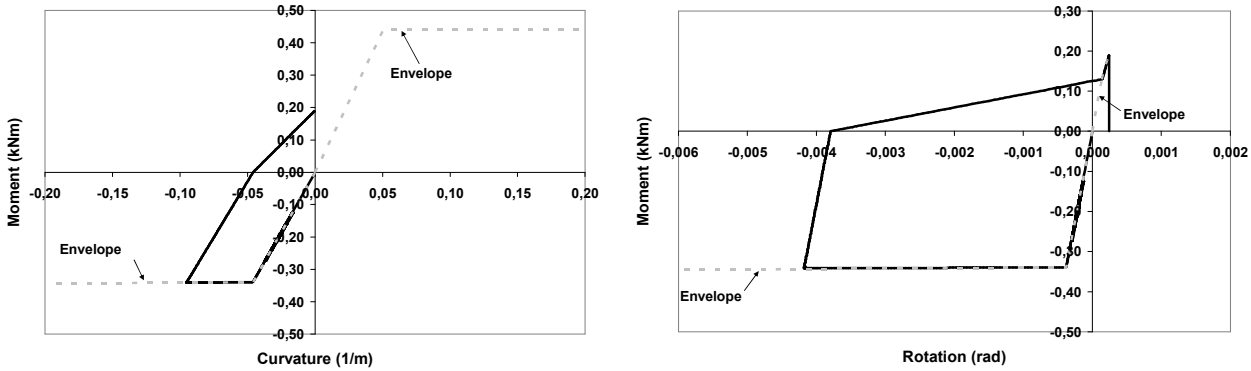


Figure 30: Hysteretic responses of left end of the 1st storey beam of the El-Attar et al. (1997) frame specimen predicted by the FSB analytical model for the 0.45g Taft acceleration record: a) M-φ; b) M-$\theta_{slip}$

The FSB analytical model predicts the anchorage failure of the positive reinforcement at the left end of the first storey beam for the 0.45g Taft earthquake motion. This is clear by Fig.

30 presenting hysteretic M-φ and M-$\theta_{slip}$ responses of this end. It can be seen that while flexural response remains at the reloading stage, M-$\theta_{slip}$ concludes the reloading branch, moves on to the positive envelope curve and finally drives to failure, exceeding ultimate anchorage moment capacity.

## 5 CONCLUSIONS

A new beam-column model is introduced for seismic damage analysis of R/C frame structures with substandard detailing. This finite element models inelastic flexural, shear, and anchorage slip deformations, as well as their interaction in an explicit manner. Hence, it is capable of simulating with accuracy the seismic response of R/C frames with inadequate detailing, where shear flexibility and fixed end rotations caused by anchorage slip usually play a vital role in their response. Additionally, it is able to predict, in the general case, brittle types of failure that cannot be precluded in structures, which do not conform to modern seismic guidelines. The numerical model is implemented in a general finite element code and it is validated against experimental results from three well documented frame specimens with brittle detailing. It is concluded that the proposed model provides accurate and reliable predictions of the frame specimen responses.

## REFERENCES


[1] E. Consenza, G. Manfredi, G.M. Verderame, Seismic assessment of gravity load designed R/C frames: Critical issues in structural modelling. *Journal of Earthquake Engineering,* **6**(1), 101-122, 2002.

[2] H. Sezen, T. Chowdhury, Hysteretic model for reinforced concrete columns including the effect of shear and axial load failure. *ASCE Journal of Structural Engineering*, **135**(2), 139-146, 2009.

[3] J. Pincheira, F. Dotiwala, J. Souza, Seismic analysis of older reinforced concrete columns. *Earthquake Spectra*, **15**(2), 245-272, 1999.

[4] P.E. Mergos, A.J. Kappos, A distributed shear and flexural flexibility model with shear-flexure interaction for R/C members subjected to seismic loading. *Earthquake Engineering and Structural Dynamics*, **37** (12), 1349-1370, 2008.

[5] P. Mergos, A.J. Kappos, Modelling gradual spread of inelastic flexural, shear and bond-slip deformations and their interaction in plastic hinge regions of R/C members. *In Proceedings of the 2nd Conference on Computational Methods in Structural Dynamics and Earthquake Engineering (COMPDYN),* Rhodes, Greece, 2009.

[6] P.E. Mergos, A.J. Kappos, Seismic damage analysis including inelastic shear-flexure interaction. *Bulletin of Earthquake Engineering*, 8(1), 27-46, 2010.

[7] P.E. Mergos, Assessment of seismic behaviour of existing R/C structures. *PhD thesis*, Aristotle University of Thessaloniki, Greece, 2010.

[8] M.V. Sivaselvan, A.M. Reinhorn, Hysteretic model for cyclic behaviour of deteriorating inelastic structures. *Technical report MCEER-99-0018*, University at Buffalo, State Univ. of New York, 1999.

[9] D. Soleimani, E.P. Popov, V.V. Bertero, Nonlinear beam model for R/C frame analysis. *Proc. Seventh Conference on Electronic Computation,* St. Louis, Misouri, 1979.

[10] H. Sezen, J.P. Moehle, Shear strength model for lightly reinforced concrete columns. *Journal of Structural Engineering*, **130**(11), 1692-1703, 2004.

[11] M.J.N. Priestley, F. Seible, R. Verma, Y. Xiao, Seismic shear strength of reinforced concrete columns. *Report No. SSRP-93/06*, University of San Diego, California, 1993.

[12] D. Biskinis, G. Roupakias, M.N. Fardis, Degradation of shear strength of R/C members with inelastic cyclic displacements. *ACI Structural Journal*, **101**(6), 773-783, 2004.

[13] R.G. Oesterle, A.E. Fiorato, J.D. Aristizabal-Ochoa, Hysteretic response of reinforced concrete structural walls. *Proc. ACISP-63: Reinforced Concrete Structures subjected to Wind and Earthquake Forces,* Detroit, 1980.

[14] M. Saatcioglu, G. Ozcebe, Response of reinforced concrete columns to simulated seismic loading. *ACI Structural Journal,* **86**(1)**,** 3-12, 1989.

[15] J.M. Alsiwat, M. Saatcioglu, Reinforcement anchorage slip under monotonic loading. *Journal of Structural Engineering*, 118(9), 2421-2438, 1992.

[16] S. Morita, T. Kaku, Slippage of reinforcement in beam-column joint of reinforced concrete framed. *Proc. 8th World Conf. on Earthquake Engineering*, Prentice-Hall, 477-484, 1984.

[17] ACI Committee 408, Bond and development of straight reinforcement in tension. American Concrete Institute, Farmington Hills, 2003.

[18] C.E.B., Model code for seismic design of concrete structures. 1990

[19] R. Park, R.A. Sampson, Ductility of reinforced concrete column sections in seismic design. *ACI Structural Journal*, **69**(9), 543-551, 1972.

[20] P. Soroushian, O. Kienuwa, M. Nagi, M. Rojas, Pullout behaviour of hooked bars in exterior beam-column connections. *ACI Structural Journal*, **85**(3), 269-276, 1988.

[21] M. Saatcioglu, J.M. Alsiwat, G. Ozcebe, Hysteretic behaviour of anchorage slip in R/C members. *Journal of Structural Engineering*, **118**(9), 2439-2458, 1992

[22] R.E. Valles, A.M. Reinhorn, S.K. Kunnath, C. Li, A. Madan, IDARC2D Version 4.0: A program for the inelastic damage analysis of buildings. *Technical Report NCEER-96-0010*, University at Buffalo, State Univ. of New York, 1996.

[23] N.M. Newmark, A Method of computation for structural dynamics. *ASCE Journal of the Engineering Mechanics Division*, **89**(1), pp. 67-94, 1959.

[24] A.E. Kanaan, G.H. Powel, DRAIN-2D: A general purpose computer program for dynamic analysis of inelastic plane structures. *Rep. EERC-73/06 and 73/22*, Univ. of California Berkeley, 1973.

[25] A.A. Golafshani, DRAIN-2D2: A program for inelastic seismic response of structures. *PhD Dissertation*, Dept. of Civil Engineering, Univ. of California Berkeley, 1982.

[26] K.V. Duong, S.A. Sheikh, F.J. Vecchio, Seismic behaviour of shear critical reinforced concrete frame: Experimental Investigation. *ACI Structural Journal,* Vol. **104**(3), 304-313, 2007.

[27] K. Elwood, J. Moehle, Dynamic collapse analysis for a reinforced concrete frame sustaining shear and axial failures. *Earthquake Engineering and Structural Dynamics*, **37**, 991-1012, 2008.

[28] A.G. El-Attar, R.N. White, P. Gergely, Behaviour of gravity load designed R/C buildings subjected to earthquakes. *ACI Structural Journal,* **94**(2), 1-13, 1997.